Journal of Materials Chemistry A

ROYAL SOCIETY OF CHEMISTRY

PAPER

View Article Online
View Journal | View Issue

Cite this: J. Mater. Chem. A, 2024, 12, 19968

Tungstic acid integrated metal–organic frameworks for efficient oxygen evolution reaction†

Zicheng Huang,[a] Wenjie Shao,[a] Yijuan Zheng,[a] Junyu Wang,[a] Mao Wang,[a] Shuang Li,[a] Xiaohui Xu,*[b] Chong Cheng *[a] and Changsheng Zhao *[a]

Received 28th April 2024
Accepted 5th June 2024

DOI: 10.1039/d4ta02924k

rsc.li/materials-a

Transition metal oxide-based catalysts are known as the most active oxygen evolution reaction (OER) catalysts due to their intrinsic electronic structures and binding strength of oxygenated intermediates. However, even the most active transition metal oxide-based OER catalysts have a turnover frequency far lower than that of the oxygen-evolving complexes in biological systems for intermolecular site aggregation. Herein, we implement the hybridization of a metal–organic framework and tungstic acid ($WO_3 \cdot xH_2O$-in-MIL-88) to achieve ordered FeNi site isolation at the molecular level and avoid intermolecular decomposition during the catalysis process. The optimized hybrid with 15% tungstic acid (15%-$WO_3 \cdot xH_2O$-in-MIL-88) achieves a much-enhanced OER activity and stability in terms of a low overpotential of 263 mV to reach a current density of 10 mA cm^{-2}, a low Tafel slope of 39 mV dec^{-1}, and long-term stability, which is much superior to that of the commercial RuO_2 catalyst.

1 Introduction

Scalable water electrolysis is a promising solution for achieving carbon-free and carbon-neutral under the urgent global warming issue.[1–5] Developing efficient and low-cost oxygen evolution reaction (OER) catalysts is a major challenge due to the four-electron coupled process and higher energy barriers.[6] Elaborately designed electrocatalysts have been proved to reduce the overpotential and sluggish kinetics at the anode effectively. Transition metal oxide-based catalysts are known as the most active due to their intrinsic electronic structures and binding strength of oxygenated intermediates.[7,8] In particularl, well-defined NiFe hydroxides treated with several different strategies, such as optimizing the Ni/Fe ratio,[9] introducing a third dopant,[10–14] or manufacturing defects,[15] are explored to be the most efficient OER catalysts. However, such transition metal oxide catalysts still have a turnover frequency (TOF) far lower than that of the oxygen-evolving manganese complexes in photosystem II in nature.[16,17] The four Mn atom complexes in biological systems are discrete and encapsulated within proteins to provide specific interactions with substrates and fast water splitting.[18,19] Hybridization of inorganic clusters and organic components into a robust framework to combine the advantages of homogeneous systems with well-isolated oxide active-sites still offers chances to break the current limitations of traditional catalysts.

Metal–organic frameworks (MOFs) are constructed by connecting inorganic secondary building units (SBUs) with organic ligands to form an infinitely three-dimensional chemical space,[20–23] which provides a unique platform to design

[a]College of Polymer Science and Engineering, State Key Laboratory of Polymer Materials Engineering, Sichuan University, Chengdu 610065, China. E-mail: chong.cheng@scu.edu.cn; zhaochsh70@scu.edu.cn

[b]Department of Ultrasound, West China Hospital, Sichuan University, Chengdu 610041, China. E-mail: xiaohuixu@scu.edu.cn

† Electronic supplementary information (ESI) available. See DOI: https://doi.org/10.1039/d4ta02924k

Chong Cheng

Chong Cheng is currently a full professor in the department of polymer science at Sichuan University. He obtained his BSc and PhD from Sichuan University. After a research stay at the University of Michigan, Ann Arbor, USA, he joined the Freie Universität Berlin as an AvH research fellow. His current scientific interests include fabricating polymer-based catalytic materials and their applications in nanomedicines, biomaterials, artificial enzymes, and electro-/thermal-/photo-catalysts; especially their molecular synthesis, atom engineering, micro-/nano-structural design, machine learning and AI-assisted material design, and cutting-edge applications. He has published over 200 SCI papers, including Nature Materials, Nature Communications, Science Advances, and Advanced Materials.

homogeneous active catalytic sites into heterogeneous catalysts due to its permanent open pores.[24–27] Pioneering studies have shown that the immobilization of the cobalt-oxo cubane core (Co_4O_4) into a MOF will stabilize the active sites and prevent them from intermolecular decomposition during OER catalysis.[28] However, MOF materials usually show poor conductivity and stability, which limits their catalytic performance.[29] Recently, numerous efforts have been made to improve the MOF conductivity and stability for electrocatalysis: combining highly conductive graphene or polymers with MOFs,[30] where the access to catalytic sites was partially blocked by the coverage, or conversion of the MOF into metal nanoparticles loaded on carbon by thermal decomposition, where the porosity and the isolation of the ordered site were compromised.[31–33] Therefore, it is critical to find a new path to improve MOF conductivity when applying it in OER catalysis and maintain its ordered structures with well-isolated catalytic sites simultaneously.

Here, we designed a facile strategy to impregnate tungsten oxide (WO_3) and its hydrate (tungstic acid, $WO_3 \cdot xH_2O$) in MOF structures to form a series of hybrids for efficient OER catalysis under alkaline and seawater conditions. Specifically, an FeNi-based MOF, MIL-88, is used for fabricating the composites with the spatial arrangement of WO_3 or $WO_3 \cdot xH_2O$. Such precise positioning of these components within the pores of the MOF structure was achieved by the encapsulation of peroxotungstic acid and sequential gelation, syneresis, and aging. The MOF backbone was well maintained during this gradual condensation of peroxotungstic acid molecules in water solution while forming the $WO_3 \cdot xH_2O$ (Scheme 1).[34,35] The amount of $WO_3 \cdot xH_2O$ can be fine-tuned by controlling the stoichiometry of the starting materials in the encapsulation process. The final products are termed n%-$WO_3 \cdot xH_2O$-in-MIL-88, where n is the weight percentage of $WO_3 \cdot xH_2O$. The one with a 15% weight percentage of $WO_3 \cdot xH_2O$, 15%-$WO_3 \cdot xH_2O$-in-MIL-88, shows the best electronic conductivity and OER catalytic performance among the series of samples with the overpotential of 263 mV at 10 mA cm^{-2} and a low Tafel slope of 39 mV dec^{-1} in 1 M KOH, which are far better than those of the commercial RuO_2 catalyst. The electrolyzer constructed based on the 15%-$WO_3 \cdot xH_2O$-in-MIL-88 catalyst only requires 1.81 V to drive a current of 250 mA cm^{-2} with good stability.

2 Materials and methods

2.1 Materials

Iron chloride hexahydrate ($FeCl_3 \cdot 6H_2O$, AR, Aladdin), nickel(II) nitrate hexahydrate ($Ni(NO_3)_2 \cdot 6H_2O$, AR, Aladdin), 1,4-benzenedicarboxylic acid (BDC, 99%, Aladdin), *N*,*N*-dimethylformamide (DMF, C_3H_7NO, 99.5%, Aladdin), tungstic acid (H_2WO_4, 99%, Aladdin), hydrogen peroxide(H_2O_2, 30%), iridium oxide powder (RuO_2, 99%, Alfa Aesar), Nafion (D520, 5 wt%, Alfa Aesar), Ketjen Black (KB), and potassium hydroxide (KOH, 85%, Aladdin) were used as received. Ultrapure water was used to prepare all aqueous solutions.

2.2 Synthesis

MIL-88-Fe/Ni was synthesized according to the reported procedure.[36,37] A mixture of 181.1 mg $FeCl_3 \cdot 6H_2O$, 96 mg $Ni(NO_3)_2 \cdot 6H_2O$, and 166.1 mg 1,4-benzene-dicarboxylic acid was combined with DMF (10 mL) in a Teflon-lined autoclave (25 mL) under continuous stirring until the solution achieved clarity. Subsequently, 2 mL NaOH (0.4 M) was added dropwise while stirring. After stirring for 15 minutes, the autoclave was transferred to a conventional oven and heated at 100 °C for 48 hours to synthesize MIL-88-Fe/Ni, referred to as MIL-88 in this article. $WO_3 \cdot xH_2O$-in-MIL-88 was synthesized according to the reported procedure.[34] First, 0.4 g of $WO_3 \cdot H_2O$ was dissolved in 10 mL of 30% H_2O_2 at 60 °C for 5 hours with continuous stirring to form a peroxotungstic precursor. Subsequently, the mixed solution was naturally cooled to room temperature before adding a specific amount of peroxotungstic acid solution and 50 mg of activated MIL-88 into a 20 mL glass bottle containing 5 mL of EtOH under continuous stirring at 24 °C for 12 hours. Finally, the solvent in the mixture was evaporated at room temperature and further aged at 80 °C for an additional period of 12 hours. The precise loading of tungstic acid is regulated by adjusting the dosage of the peroxotungstic acid solution (Table S1†).

2.3 Characteristic measurements

Scanning electron microscopy (SEM) images were obtained by using a Hitachi Regulus 8220, Japan; the elemental mapping is

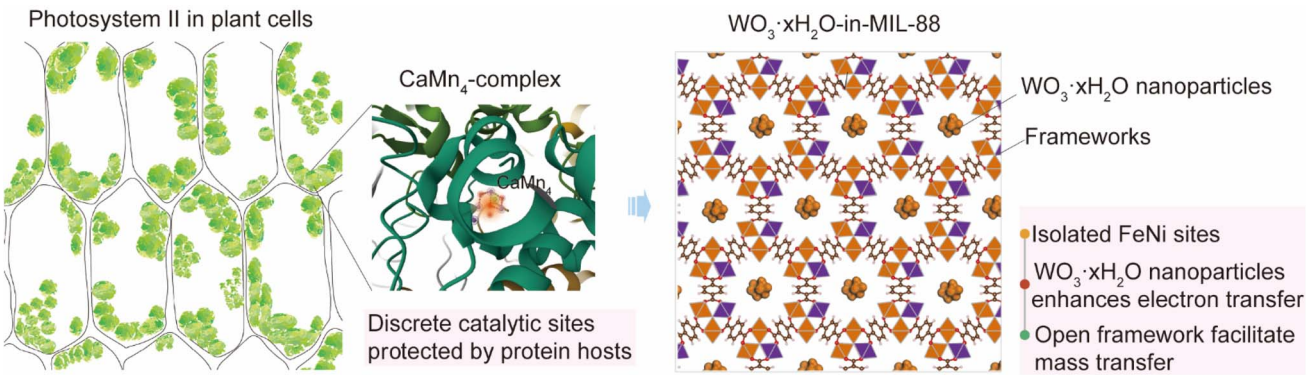

Scheme 1 Illustration of the materials design. Mimicking the isolated and encapsulated active manganese sites within proteins in nature through the integration of NiFe sites and tungstic acid nanoparticles in an ordered open framework in an isolated manner.

obtained from an energy-dispersive X-ray detector (Quantax FlatQUAD, Bruker). The platinum coating was deposited with a layer of about 1 nm. Transmission electron microscopy (TEM) was performed with a Tecnai G2 F20 S-TWIN operated at 200 kV. X-ray diffraction (XRD) measurements were performed by using an Empyrean PIXcel3D with Co Kα irradiation and a Rigaku Ultima IV with Cu Kα irradiation. X-ray photoelectron spectroscopy (XPS) measurements were performed on a K-Alpha™ + X-ray photoelectron spectrometer (Thermo Scientific) with a hemispheric 180° dual-focus analyzer with a 128-channel detector and monochromatic Al Kα irradiation. Thermogravimetric analysis of 15%-$WO_3 \cdot xH_2O$-in-MIL-88 and 15%-WO_3-in-MIL-88 composites was performed on a thermogravimetric analyzer with samples held in aluminum oxide pans. The heating temperature ranged from 25 °C to 800 °C at a constant heating rate of 5 °C min^{-1} with an airflow rate of 20.0 mL min^{-1}. Ar was used in this measurement as both balance gas and sample gas.

3 Results and discussion

3.1 Synthesis and morphological characterization

MIL-88 with the FeNi bi-component was synthesized using a solvothermal method by mixing iron chloride hexahydrate, nickel chloride hexahydrate, and 1,4-benzene dicarboxylic acid in *N*,*N*-dimethyl-formamide.[36] Fig. 1a shows the uniform spatial arrangements of Fe and Ni atoms in the MIL-88 structure. The scanning electron microscopy (SEM) image shows a typical spindle structure for MIL-88, which was selected as the substrate to encapsulate $WO_3 \cdot xH_2O$ (Fig. 1b). We applied the sol–gel chemistry to gradually grow $WO_3 \cdot H_2O$ in the confined space of MIL-88.[34] Sequentially, the prepared $WO_3 \cdot H_2O$ is dissolved in H_2O_2 to form a homogeneous aqueous solution of the peroxotungstic acid precursor. Then, different amounts of peroxotungstic acid solution were mixed with MIL-88 in ethanol under continuous stirring for gradual gelation for 12 h. The gels were then aged at 80 °C to obtain the *n*%-$WO_3 \cdot xH_2O$-MIL-88 samples. The SEM images in Fig. 1c–e reveal similar spindle structures of 7%-$WO_3 \cdot xH_2O$-MIL-88, 15%-$WO_3 \cdot xH_2O$-MIL-88, and 30%-$WO_3 \cdot xH_2O$-MIL-88 with that of the original MIL-88, indicating that the impregnation of $WO_3 \cdot H_2O$ does not change the morphology of MIL-88. Furthermore, it can be seen that after the introduction of up to 30% $WO_3 \cdot H_2O$ into the pores, the crystal surface is still as smooth as the original MIL-88, which could be evidence that the $WO_3 \cdot H_2O$ is growing inside the pores of MIL-88 rather than on the surface. When the loading content increases to 50%, it far exceeds the pore capacity, the morphology of the MIL-88 cannot be well maintained, and large particles are observed in SEM images (Fig. S1†). Energy-dispersive X-ray spectroscopy (EDS) mapping analysis by SEM demonstrated the uniform distribution of Fe, Ni, O, and W elements in the MIL-88 and *n*%-$WO_3 \cdot xH_2O$-in-MIL-88 samples. In particular, the evenly distributed W signal within the entire MIL-88 structure strongly supports the inclusion of $WO_3 \cdot H_2O$ in the pores (Fig. S2–S6†).

Powder X-ray diffraction (PXRD) was conducted to investigate the crystal structures. With increasing the loading amount of $WO_3 \cdot xH_2O$ from 7% to 15%, the crystal structure of MIL-88 can be well maintained. The decrease in peak intensity happens when 30% $WO_3 \cdot xH_2O$ is introduced, and the crystal structure is destroyed for 50%-$WO_3 \cdot xH_2O$-MIL-88 (Fig. 1f). It is worth noting that the (101) reflection for MIL-88 shifted from 10.36° to 10.60° when 15% $WO_3 \cdot H_2O$ was introduced (15%-$WO_3 \cdot xH_2O$-MIL-88), which indicates the slight lattice contraction for MIL-88.[38–40] Such lattice shrinkage indicates the close interactions between $WO_3 \cdot H_2O$ nanoparticles and the MIL-88 backbone. Transition electron microscopy (TEM) was further employed to characterize the crystal structures of MIL-88 and 15%-$WO_3 \cdot xH_2O$-in-MIL-88, which first revealed the similar uniform spindle-shaped crystals with 60–80 nm in width and 200–400 nm in length for MIL-88 and 15%-$WO_3 \cdot xH_2O$-in-MIL-88 (Fig. S7†). High-resolution TEM images show clear lattice fringes of the (101) plane with *d*-spacings of 0.945 nm for MIL-88 and 0.937 nm for 15%-$WO_3 \cdot xH_2O$-in-MIL-88 (Fig. 1g and h), which confirms the lattice shrinkage observed in PXRD results. TEM elemental mapping reveals again the uniformly distributed Fe and Ni elements in MIL-88 and Fe, Ni, and W elements in 15%-$WO_3 \cdot xH_2O$-in-MIL-88 (Fig. 1i–l and S8†), which evidences the inclusion of $WO_3 \cdot xH_2O$ nanoparticles into the pores.

3.2 Elemental analysis

To further investigate the components and electronic state of the synthesized samples, X-ray photoelectron spectroscopy (XPS) has been conducted. As shown in the survey spectra, the presence of Ni, Fe, O, and C in the MIL-88 can be confirmed, while clear W peaks were observed for *n*%-$WO_3 \cdot xH_2O$-in-MIL-88, revealing the successful loading of $WO_3 \cdot xH_2O$ in MIL-88 (Fig. 2a, b and S9 and Table S3†). As shown in Fig. 2c and S10,† the Fe 2p spectrum of MIL-88 and $WO_3 \cdot xH_2O$-in-MIL-88 both exhibits a mixture of Fe^{2+} and Fe^{3+} valences, and the peaks at 709.8 eV and 713.2 eV can be indexed to Fe^{2+} and Fe^{3+}. For MIL-88, the Ni 2p spectrum shows an apparent 2p3/2 peak at 855.1 eV, which is the characteristic peak of Ni^{2+} and was increased to 855.3 eV in $WO_3 \cdot xH_2O$-in-MIL-88 ($\Delta E = 0.15$ eV) (Fig. 2d and S11†). The O 1s region of MIL-88 consists of organic C–O (530.8 eV), organic C═O (533.0 eV), and metal oxides (528.5 eV), with a calculated metal oxide peak area ratio of 0.022 (Fig. 2e). After loading $WO_3 \cdot xH_2O$, the peak area ratio of oxides increases to 5.9% in 7%-$WO_3 \cdot xH_2O$-in-MIL-88, 6.2% in 15%-$WO_3 \cdot xH_2O$-in-MIL-88, 12.2% in 30%-$WO_3 \cdot xH_2O$-in-MIL-88, and 34.8% in 50%-$WO_3 \cdot xH_2O$-in-MIL-88 (Fig. S12†). In the W 4f region, a peak at 34.6 eV indicates that the W element distributed inside the channel is in the form of tungstic acid (Fig. 2f and S13†).

3.3 Electrocatalytic activity toward the OER in 1 M KOH

The electrocatalytic performance of *n*%-$WO_3 \cdot xH_2O$-in-MIL-88 composites for the OER is first measured *via* a three-electrode configuration with rotating disk electrodes.[41,42] The OER performance of MIL-88 was also assessed for comparison in an identical environment. As shown by the linear sweep voltammetry (LSV) curves in Fig. 3a, the MIL-88 requires an

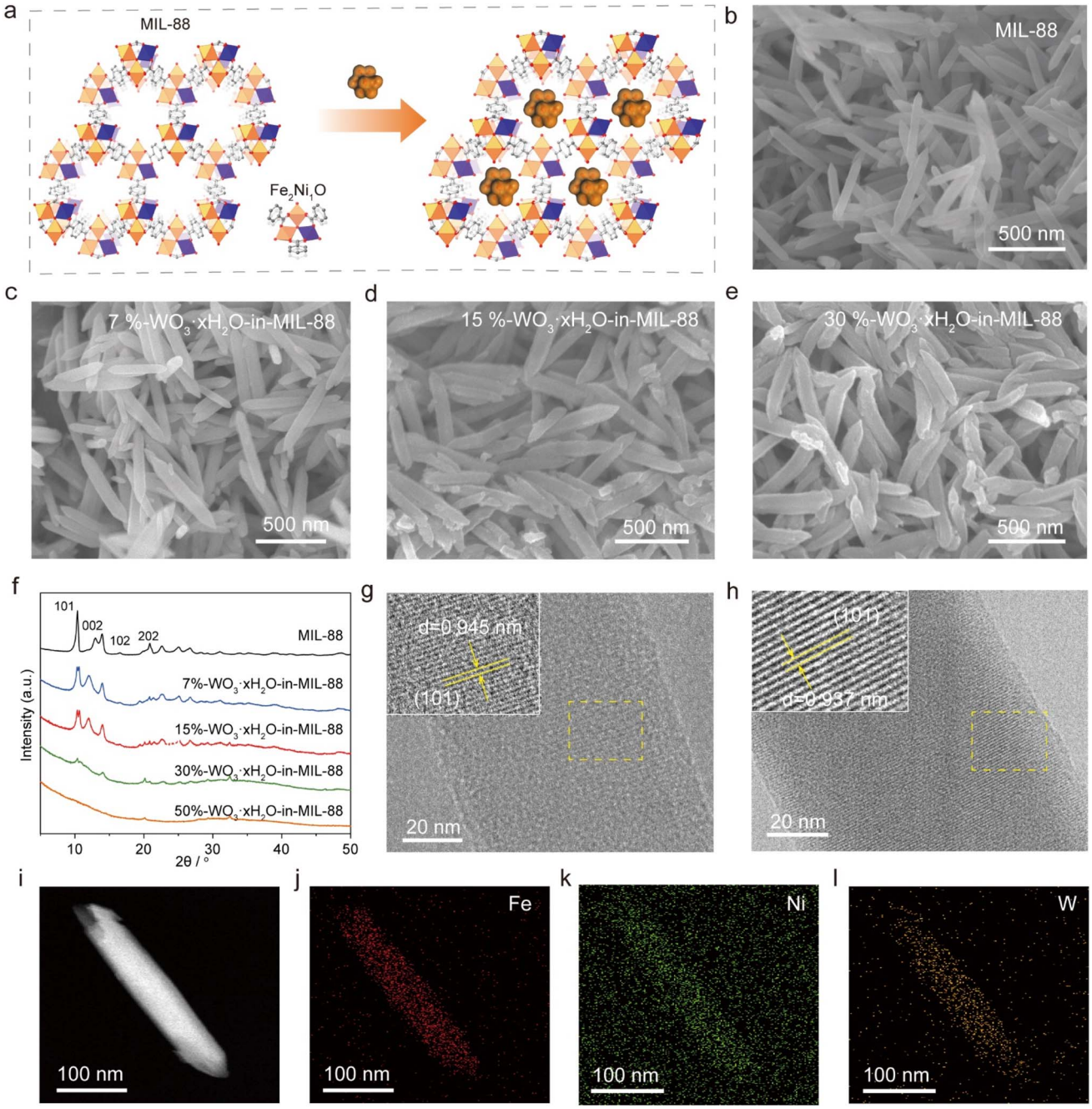

Fig. 1 (a) Illustration of the hybridization of $WO_3 \cdot H_2O$ into MIL-88 pores. SEM images of the as-synthesized (b) MIL-88, (c) 7%-$WO_3 \cdot xH_2O$-in-MIL-88, (d) 15%-$WO_3 \cdot xH_2O$-in-MIL-88, and (e) 30%-$WO_3 \cdot xH_2O$-in-MIL-88. (f) XRD patterns of the series of $WO_3 \cdot xH_2O$-in-MIL-88 samples collected using the Co target X-ray source ($\lambda = 1.789$ Å). Transmission electron microscopy (TEM) images of (g) MIL-88 and (h) 15%-$WO_3 \cdot xH_2O$-in-MIL-88. (i–l) The corresponding elemental mapping of 15%-$WO_3 \cdot xH_2O$-in-MIL-88 from TEM.

overpotential of 297 mV to reach a current density of 10 mA cm^{-2}, while it can be largely reduced to 270 mV by introducing 7% $WO_3 \cdot xH_2O$. The best performance can be reached at 15% $WO_3 \cdot xH_2O$; the 15%-$WO_3 \cdot xH_2O$-in-MIL-88 catalysts show the lowest overpotential of 263 mV to reach a current density of 10 mA cm^{-2}, which is even better than that of the 30%-$WO_3 \cdot xH_2O$-in-MIL-88 (279 mV), 50%-$WO_3 \cdot xH_2O$-in-MIL-88 (300 mV), and commercial noble-metal based RuO_2 catalysts (270 mV) (Fig. S14†). The outstanding OER performance of 15%-$WO_3 \cdot xH_2O$-in-MIL-88 was further confirmed by its substantially lower Tafel slope (39 mV dec^{-1}) than those of RuO_2 (50 mV dec^{-1}), MIL-88 (46 mV dec^{-1}), 7%-$WO_3 \cdot xH_2O$-in-MIL-88 (40 mV dec^{-1}), 30%-$WO_3 \cdot xH_2O$-in-MIL-88 (44 mV dec^{-1}), and 50%– WO_3-$\cdot xH_2O$-in-MIL-88 (60 mV dec^{-1}) (Fig. 3b). Taking the catalyst loading into consideration for practical applications, the mass activities of the n%-$WO_3 \cdot xH_2O$-in-MIL-88 and MIL-88 were evaluated by normalizing the LSV curves with the mass of Fe + Ni. As depicted in Fig. 3c, the n%-$WO_3 \cdot xH_2O$-in-MIL-88 catalyst

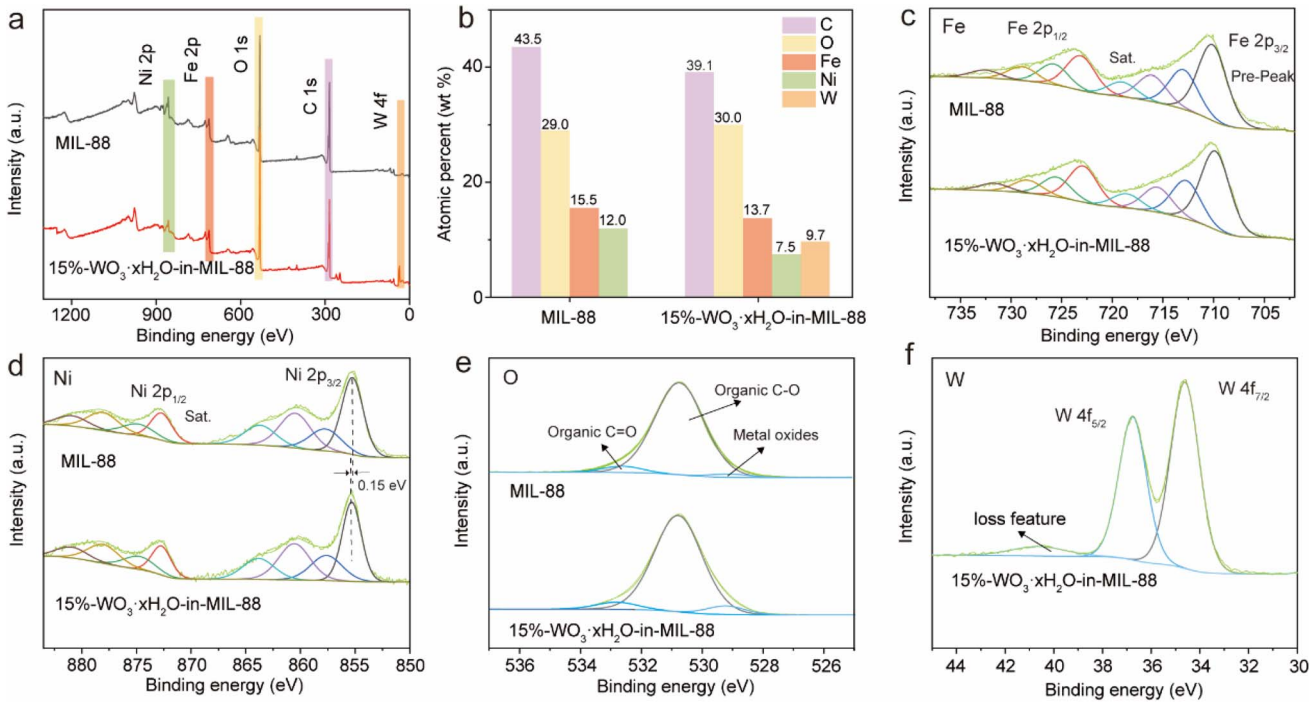

Fig. 2 (a) XPS survey scans of MIL-88 and 15%-$WO_3 \cdot xH_2O$-in-MIL-88. (b) Atom ratios of MIL-88 and 15%-$WO_3 \cdot xH_2O$-in-MIL-88. XPS spectra of (c) Fe 2p, (d) Ni 2p, (e) O 1s, (f) W 4f.

exhibits an extraordinarily efficient mass activity of 190.6 A g_{FeNi}^{-1} at an over-potential of 300 mV, which is 5 times higher than that of MIL-88 (36.0 A g_{FeNi}^{-1}) and higher than that of RuO_2 (117.6 A g^{-1}). The turnover frequency (TOF) is calculated to evaluate the intrinsic activity of each Fe/Ni atom. The highest TOF value is obtained for 15%-$WO_3 \cdot xH_2O$-in-MIL-88 as 0.135 s^{-1}, which is higher than that of 7%-$WO_3 \cdot xH_2O$-in-MIL-88 (0.112 s^{-1}), 30%-$WO_3 \cdot xH_2O$-in-MIL-88 (0.091 s^{-1}), and 50%-$WO_3 \cdot xH_2O$-in-MIL-88 (0.0519 s^{-1}) and MIL-88 (0.022 s^{-1}) (Fig. 3d). This result further ascertains the highest OER performance of 15%-$WO_3 \cdot xH_2O$-in-MIL-88.

In addition, we investigated the double-layer capacitances (C_{dl}) of the catalysts to evaluate electrochemically active surface areas (ECSAs) (Fig. S15†). The similar C_{dl} of 7%-$WO_3 \cdot xH_2O$-in-MIL-88, 15%-$WO_3 \cdot xH_2O$-in-MIL-88, and 30%-$WO_3 \cdot xH_2O$-in-MIL-88 indicates their similar ECSA for electrocatalysis (1.67 mF cm^{-2} for 7%-$WO_3 \cdot xH_2O$-in-MIL-88, 30%, 1.70 mF cm^{-2} for 15%-$WO_3 \cdot xH_2O$-in-MIL-88, and 1.47 mF cm^{-2} for 30%-WO_3-$\cdot xH_2O$-in-MIL-88). Electrochemical impedance spectroscopy (EIS) was used to investigate the electron/proton transfer at the interface between the catalyst and electrolyte (Fig. S16 and Table S4†). 15%-$WO_3 \cdot xH_2O$-in-MIL-88 has an appropriate loading content to form an ideal intermingled structure to feature the lowest electrochemical impedance among all the series of samples, indicating the fastest charge transfer, while its porosity is well maintained. Thus, 15%-$WO_3 \cdot xH_2O$-in-MIL-88 is able to facilitate both charge transfer and mass transfer during catalysis to achieve better catalytic performance. It can be concluded that the accurate filling of MIL-88 with 15% $WO_3 \cdot xH_2O$ leads to superior catalytic activity as evidenced by its lowest overpotential, smallest Tafel slope, and highest mass activity among other comparative catalysts and most of the currently reported catalysts (Fig. 3e and f and Table S5†). Furthermore, chronopotentiometry measurements were employed to assess the durability of the 15%-$WO_3 \cdot xH_2O$-in-MIL-88 catalyst on carbon cloth, which exhibited more than 100 hours of stability at constant working current densities of 10 mA cm^{-2} and 50 mA cm^{-2} (Fig. 3g). The oxidation state of both Ni and Fe slightly changed after the stability test, which was indicated by the marginal shifts in their XPS spectra (Fig. S17†). It can be seen that the overall deposition of catalysts on carbon cloth doesn't change too much, however, the shape of catalysts themselves slightly changes from needle-shape to cross-linked particles (Fig. S18†). The slightly increased Fe and Ni content and decreased W content indicate the formation of an active Fe, Ni oxide layer on the surface of the catalyst (Table S6†).

3.4 Activity mechanism study

To investigate the roles and mechanisms of $WO_3 \cdot H_2O$ enhanced OER activity, a series of control experiments and theoretical analysis were conducted. First, the H_2O_2-treated MIL-88 shows a much-decreased OER activity with an over-potential of up to ~340 mV, indicating that the performance enhancement can be attributed to the $WO_3 \cdot H_2O$ (Fig. S19, Table S2†). The diffusion of water molecules to have close contact with catalytic sites is critical for the OER kinetics.[43,44] The inclusion of $WO_3 \cdot H_2O$ will hugely influence the water molecule diffusion within MOF pores by improving the hydrophilicity of the composites. Fourier-transform infrared (FTIR) spectra of MIL-

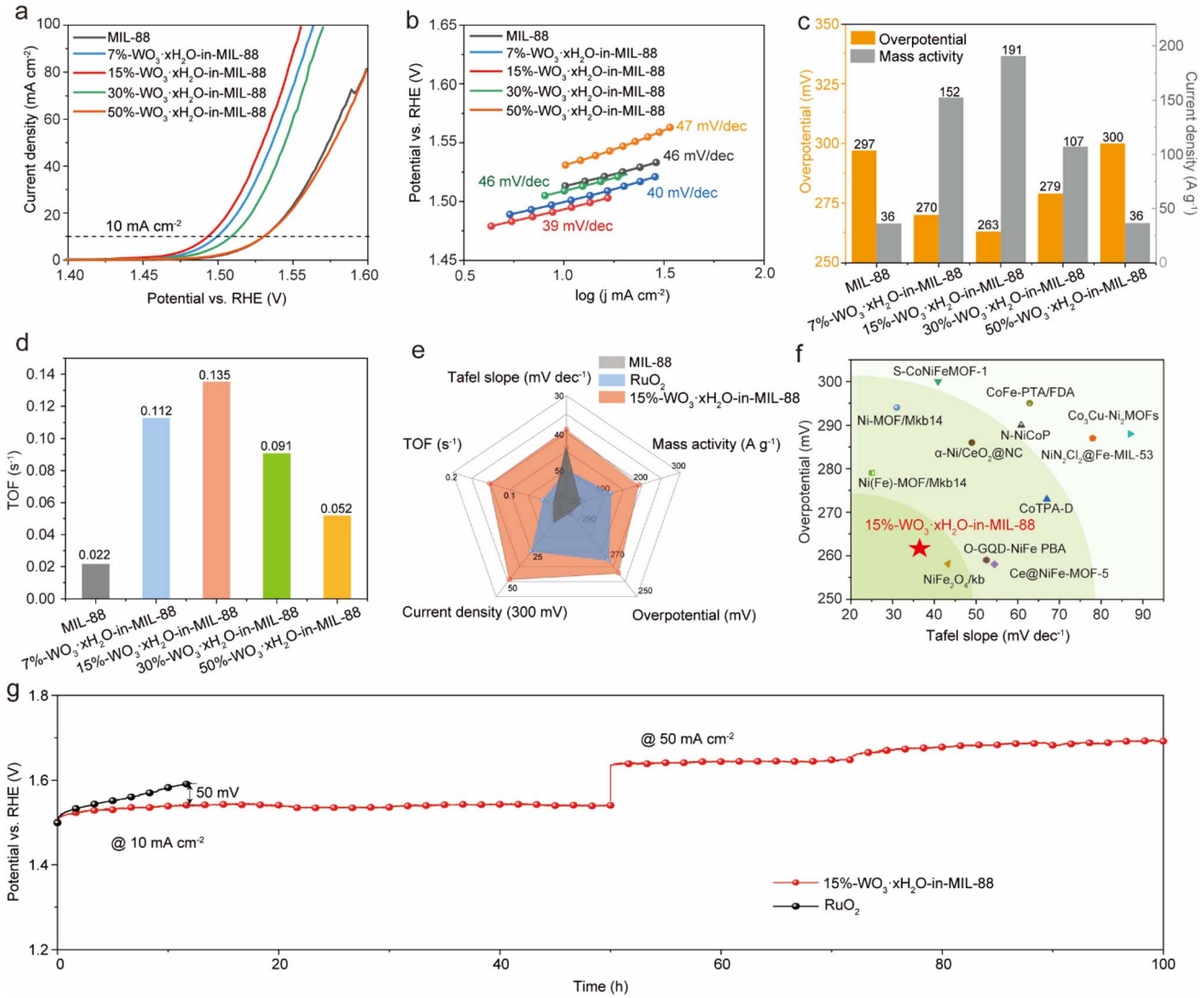

Fig. 3 (a) OER polarization curves and (b) Tafel plots of MIL-88 and the series of $WO_3 \cdot xH_2O$-in-MIL-88 in 1 M KOH. (c) Comparison of overpotentials at 10 mA cm^{-2} and mass current densities and (d) TOF values at an overpotential of 300 mV. Overall evaluation of the OER performance (e) comparison with synthesized catalysts and (f) comparison with reported OER catalysts. (g) Long-term stability test of 15%-$WO_3 \cdot xH_2O$-in-MIL-88 and RuO_2 performed at a current density of 10 mA cm^{-2}.

88 and $WO_3 \cdot xH_2O$-in-MIL-88 indicate that the water peak shows a significant increase when the framework structure remains consistent (Fig. S20†). As indicated by the thermal gravimetric analysis (TGA) results, the coordinated water in the crystal can be well removed before 150 °C (Fig. S21†).[34] We then treated the 15%-$WO_3 \cdot xH_2O$-in-MIL-88 catalyst under 150 °C to synthesize the control sample 15%-WO_3-in-MIL-88, while the water peak in FTIR weakened significantly, and the morphology remained unchanged (Fig. 4a, b, S22 and S23†). The much lower OER performance of 15%-WO_3-in-MIL-88 in terms of higher overpotential (280 mV) and much higher Tafel slope (90 mV dec^{-1}) than that of 15%-$WO_3 \cdot xH_2O$-in-MIL-88 (Fig. 4c and S24†) indicates the crucial roles of the coordinated water in OER catalysis. The water contact angle experiments are conducted to evaluate the surface hydrophilicity, where 15%-$WO_3 \cdot xH_2O$-in-MIL-88 shows a much smaller contact angle of 25° than that of MIL-88 (67°) and 15%-WO_3-in-MIL-88 (60°), indicating the best hydrophilicity for 15%-$WO_3 \cdot xH_2O$-in-MIL-88 (Fig. 4d).[43,44] Raman spectroscopy results suggested the *in situ* formation of Fe–O–O–Ni during electrooxidation, where molecular water adsorption is essential (Fig. 4e).[45] To better understand how the water molecules diffuse inside the catalysts, we carry out molecular dynamics (MD) simulation (Fig. 4f). We first build two supercells of 15%-$WO_3 \cdot xH_2O$-in-MIL-88 and 15%-WO_3-in-MIL-88 that are filled with a certain number of water molecules, respectively (Fig. S25†). As evident from Fig. 4g and h, the average metal–water (Fe/Ni) distance in MIL-88 with $WO_3 \cdot xH_2O$ is noticeably shorter, as reflected by a reduced position at the initial peak in the radial distribution function ($g(r)$) (Fig. S26†). This implies a heightened affinity between 15%-$WO_3 \cdot xH_2O$-in-MIL-88 and water molecules, suggesting a more favorable interaction. This increased affinity could be the main

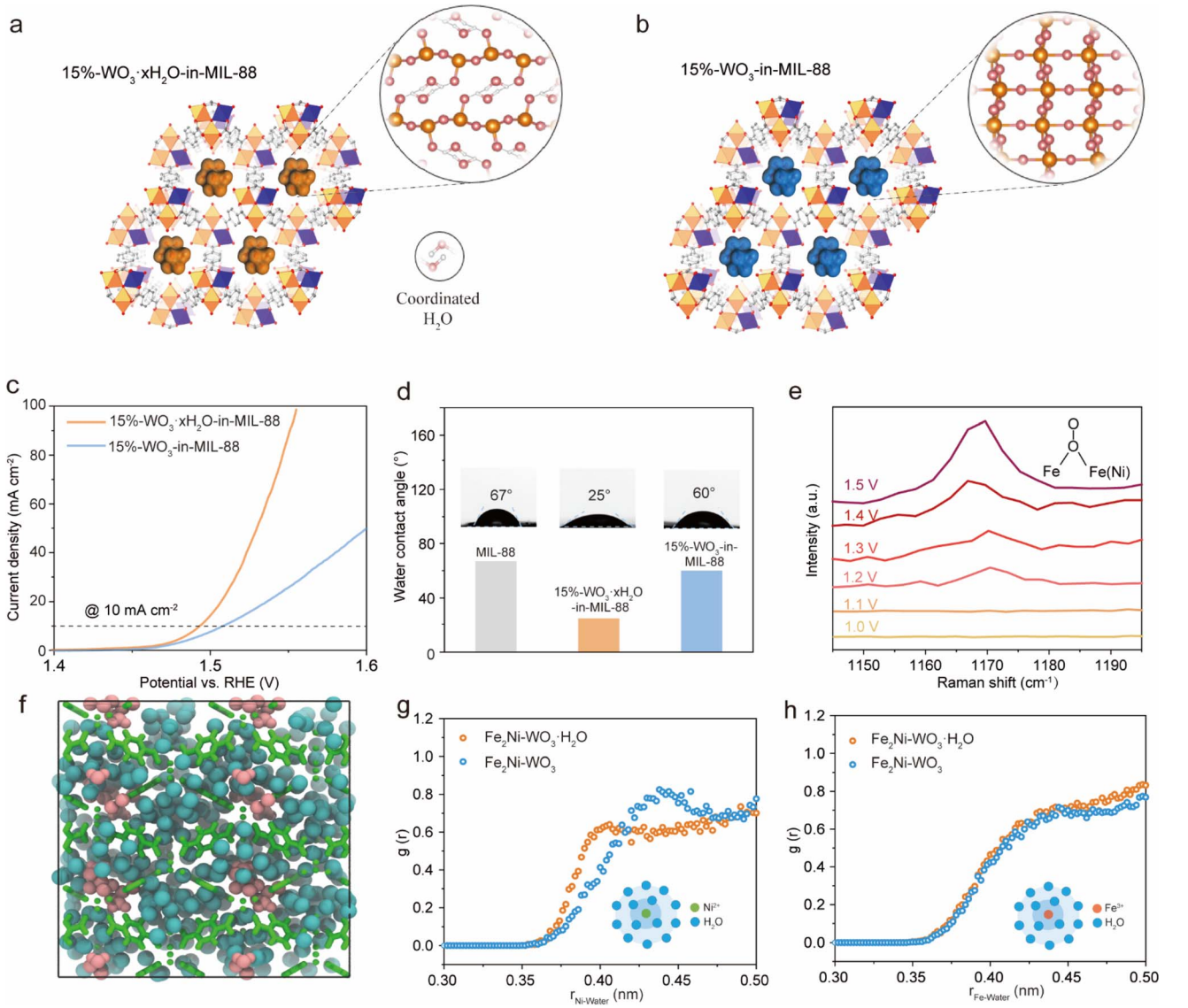

Fig. 4 (a and b) Structure illustration of $WO_3 \cdot H_2O$ and WO_3 nanoparticles in MIL-88. (c) The polarization curves of 15%-$WO_3 \cdot xH_2O$-in-MIL-88 and 15%-WO_3-in-MIL-88. (d) The water contact angle of different catalysts. (e) The *in situ* Raman spectra of 15%-$WO_3 \cdot xH_2O$-in-MIL-88 during OER catalysis. (f) The simulation illustration shows MIL-88 cavities filled with water molecules (blue spheres). For clarity, MIL-88 is shown as a green wireframe. WO_3 or $WO_3 \cdot H_2O$ is represented by red spheres. (g and h) Radial distribution function $g(r)$ of water molecules around Fe and Ni atoms in 15%-$WO_3 \cdot xH_2O$-in-MIL-88.

contribution to the improved OER performance of 15%-$WO_3 \cdot xH_2O$-in-MIL-88.

3.5 Electrocatalytic activity toward the OER in alkaline seawater

Such a water molecule enriched microenvironment in the pores of 15%-$WO_3 \cdot xH_2O$-in-MIL-88 could also benefit the OER performance under complicated ion conditions, for example, seawater. Therefore, initial trials were made to extend the applications of the 15%-$WO_3 \cdot xH_2O$-in-MIL-88 catalyst for the OER in alkaline seawater. As shown in Fig. 5a, the OER polarization curves indicate that the MIL-88 requires an overpotential of 390 mV to reach a current density of 10 mA cm^{-2}, while it can be largely reduced by introducing $WO_3 \cdot xH_2O$. The best performance can be reached at 15% $WO_3 \cdot xH_2O$; the 15%-$WO_3 \cdot xH_2O$-in-MIL-88 catalysts show the lowest overpotential of 360 mV to reach a current density of 10 mA cm^{-2}, which is much better than that of the 30%-$WO_3 \cdot xH_2O$-in-MIL-88, 50%-$WO_3 \cdot xH_2O$-in-MIL-88, and commercial RuO_2 catalysts (Fig. S27 and S28†). The outstanding OER performance of 15%-$WO_3 \cdot xH_2O$-in-MIL-88 in alkaline seawater was further confirmed by its substantially lower Tafel slope (59.4 mV dec^{-1}) than MIL-88 (86.4 mV dec^{-1}) (Fig. 5b and c). As shown in Fig. 5d, 15%-$WO_3 \cdot xH_2O$-in-MIL-88 shows TOF values of 0.115 s^{-1} at an overpotential of 400 mV, which is higher than that of MIL-88 (0.030 s^{-1}). Remarkably, the 15%-$WO_3 \cdot xH_2O$-in-MIL-88 catalyst enables stable oxygen

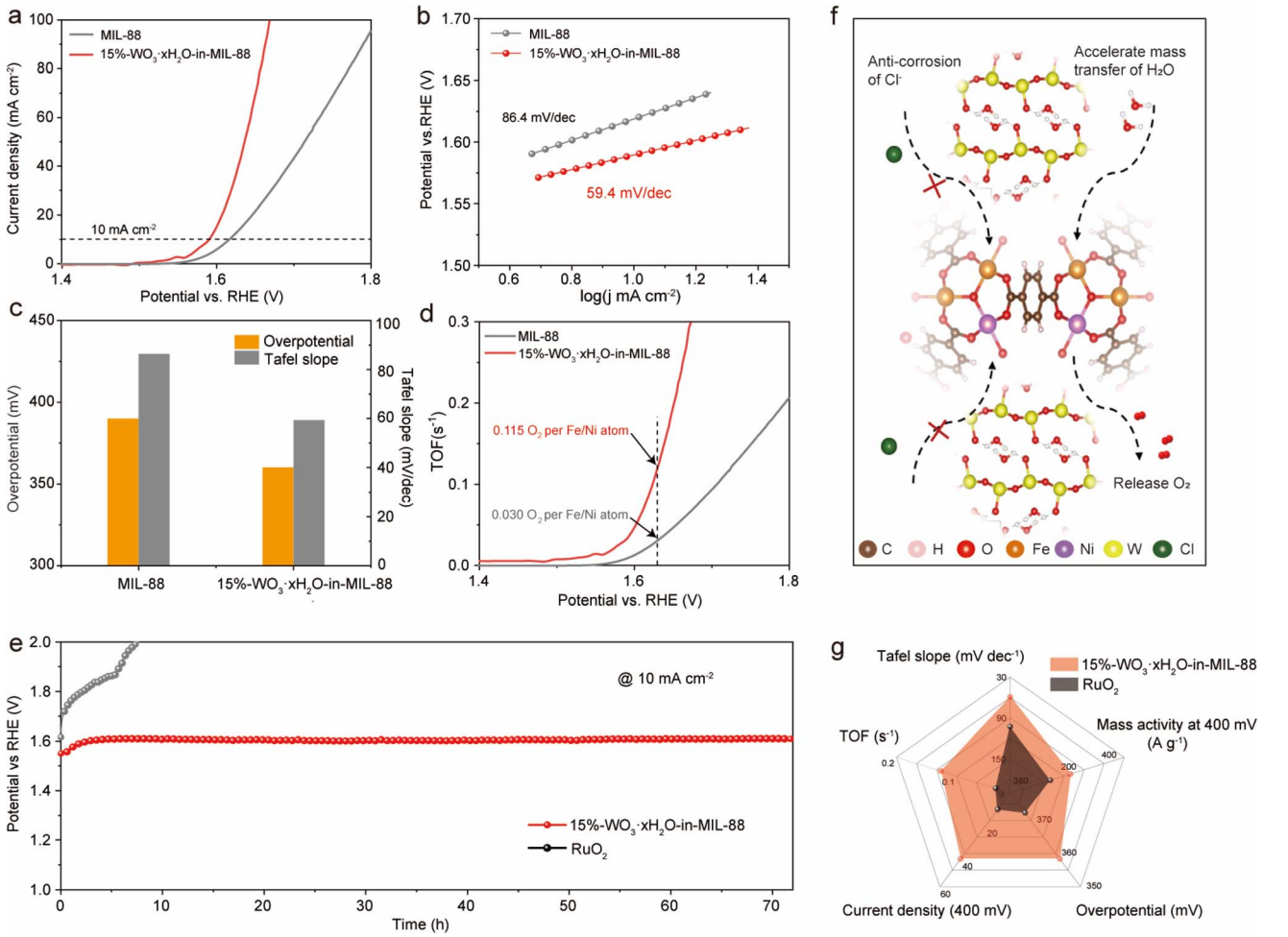

Fig. 5 (a) OER polarization curves, (b) the Tafel plots, (c) overpotentials and the Tafel slope, and (d) TOF values of MIL-88 and 15%-$WO_3 \cdot xH_2O$-in-MIL-88 in alkaline seawater. (e) Stability of 15%-$WO_3 \cdot xH_2O$-in-MIL-88 and RuO_2 in alkaline seawater at a current density of 10 mA cm^{-2}. (f) The scheme of the anti-corrosion mechanism in alkaline seawater. (g) The overall evaluation of OER performance in alkaline seawater.

production in alkaline seawater for over 70 hours at 10 mA cm^{-2} due to the effective resistance of Cl^- poisoning on active Fe/Ni sites by tungstic acid nanoparticles within MOF pores (Fig. 5e–g).[46] Such long-term stability offers promising potential for practical application.

3.6 Practical application of the catalyst

The overall water-splitting performance in an alkaline electrolyte was assessed using a two-electrode device. The anode was fabricated with 15%-$WO_3 \cdot xH_2O$-in-MIL-88 supported on a nickel foam (NF) substrate, while the cathode was commercial Pt/C supported on a NF substrate (referred to as 15%-$WO_3 \cdot xH_2O$-in-MIL-88/NF||Pt/C/NF). For comparison, the overall water-splitting performance of RuO_2/NF||Pt/C/NF made from commercial catalysts was also tested in 1 M KOH. According to Fig. 6a, the polarization curves found that a voltage of only 1.50 V is required for delivering a current density of 10 mA cm^{-2} with the 15%-$WO_3 \cdot xH_2O$-in-MIL-88/NF||Pt/C/NF setup. Moreover, only a low voltage of 1.91 V was needed for driving a current density of 100 mA cm^{-2}. Notably, the device based on 15%-$WO_3 \cdot xH_2O$-in-MIL-88/NF||Pt/C/NF exhibits excellent operation stability at 100 mA cm^{-2} for over 24 h without any noticeable decline in performance (Fig. 6b). Due to its outstanding overall water-splitting activity, this electrolyzer can be powered with a standard AA battery operating at room temperature (Fig. 6c). Compared to other reported water electrolyzers (Fig. 6d and Table S7†), such as Cu@NiFe LDH||Cu@NiFe LDH (1.54 V),[47] Ni/Ni_8P_3||Ni/Ni_8P_3 (1.61 V),[48] CoFeZr oxides||CoFeZr oxides (1.63 V),[49] *etc.*, the cell voltage requirement for achieving a current density of 10 mA cm^{-2} is much lower in our proposed configuration (15%-$WO_3 \cdot xH_2O$-in-MIL-88/NF||Pt/C/NF). To assess the practical viability of the catalyst, the membrane electrode assembly (MEA) electrolyzer was also tested by employing 15%-$WO_3 \cdot xH_2O$-in-MIL-88 as the OER catalyst (Fig. 6e). At a temperature of 25 °C, the electrolyzer achieves a current density of 250 mA cm^{-2} at a cell voltage of 1.81 V and more than 24 h stability, outperforming RuO_2/CP||Pt/C/CP (2.27 V) (Fig. 6f and g). These findings highlight the potential practical application prospects of 15%-$WO_3 \cdot xH_2O$-in-MIL-88.

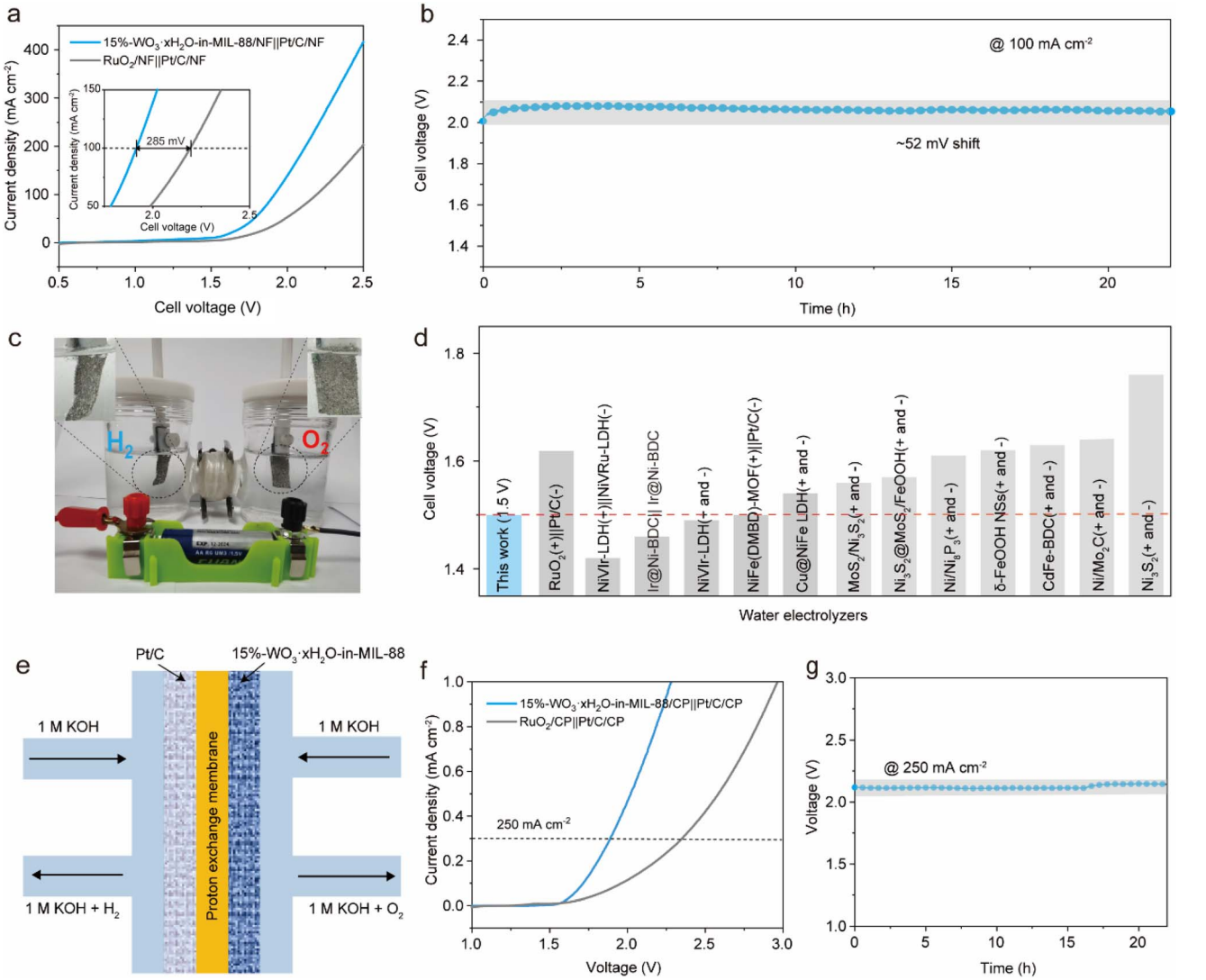

Fig. 6 (a) The polarization curves, (b) long-time stability at 100 mA cm^{-2} of 15%-$WO_3 \cdot xH_2O$-in-MIL-88/NF||Pt/C/NF and RuO_2/NF||Pt/C/NF toward overall water splitting in a H type cell. (c) The photo of the H-type cell driven by a 1.5 V AA battery. (d) Comparison of the cell voltage at 10 mA cm^{-2} with reported results. (e) The scheme of a simple MEA electrolyzer. (f) Polarization curves and (g) stability tests at 250 mA cm^{-2} of the MEA equipped with 15%-$WO_3 \cdot xH_2O$-in-MIL-88/CP||Pt/C/CP.

4 Conclusion

In summary, we report a facile synthesis strategy to integrate active FeNi sites and tungstic acid nanoparticles into an ordered open framework in an isolated manner for efficient OER catalysis by mimicking the nature of discrete manganese oxo-complexes encapsulated by proteins in photosystem II. The synergy between precisely positioned tungstic acid and the MIL-88 structure brings hydrophilic FeNi active sites in the framework, leading to an efficient electron transfer and fast reactive substrate diffusion. The composite, 15%-$WO_3 \cdot xH_2O$-in-MIL-88, exhibits a low overpotential of 263 mV at 10 mA cm^{-2} and a low Tafel slope of 39 mV dec^{-1}, which are much better than those of the commercial noble-metal RuO_2 catalyst. Notably, the catalyst shows a remarkable 72 h long-term operating stability in alkaline seawater. Further studies explored the practical potential of using this catalyst in membrane electrode assembly and a water-splitting device. This work offers new insights for the design of OER catalysts based on crystalline porous materials.

Data availability

The data that support the findings of this study are available from the corresponding author upon reasonable request.

Conflicts of interest

The authors declare no conflict of interest.

Acknowledgements

This work was financially supported by the National Natural Science Foundation of China (No. 52273269 and 82302224) and the Sichuan Science and Technology Program (No.

2023YFH0027, 2023YFH0008 and 2024YFHZ0270). We acknowledge the financial support from Fundamental Research Funds for the Central Universities and the State Key Laboratory of Polymer Materials Engineering (Grant No. sklpme2022-3-07 and sklpme2021-4-02). We gratefully acknowledge Dr Mi Zhou, Dr Chao He, and Dr Xiaorong Sun at Sichuan University for their experimental assistance.

References

1 M. F. Lagadec and A. Grimaud, *Nat. Mater.*, 2020, **19**, 1140–1150.
2 A. Ozden, F. P. García de Arquer, J. E. Huang, J. Wicks, J. Sisler, R. K. Miao, C. P. O'Brien, G. Lee, X. Wang, A. H. Ip, E. H. Sargent and D. Sinton, *Nat Sustainability*, 2022, **5**, 563–573.
3 G. S. Cassol, C. Shang, A. K. An, N. K. Khanzada, F. Ciucci, A. Manzotti, P. Westerhoff, Y. Song and L. Ling, *Nat. Commun.*, 2024, **15**, 2617.
4 Y. Wei, M. Zheng, W. Zhu and H. Pang, *Carbon Neutralization*, 2023, **2**, 271–299.
5 B. Zhang, Y. Zheng, Z. Xing, Z. Wu, C. Cheng, T. Ma and S. Li, *J. Mater. Chem. A*, 2024, **12**, 4484–4491.
6 L. Sun, M. Feng, Y. Peng, X. Zhao, Y. Shao, X. Yue and S. Huang, *J. Mater. Chem. A*, 2024, **12**, 8796–8804.
7 C. Ahn, A. Cavalleri, A. Georges, S. Ismail-Beigi, A. J. Millis and J.-M. Triscone, *Nat. Mater.*, 2021, **20**, 1462–1468.
8 M. Cheng, Z. Xing, R. Yan, Z. Zhao, T. Ma, M. Zhou, X. Liu, S. Li and C. Cheng, *InfoMat*, 2022, **5**, e12387.
9 C. W. Liang, P. C. Zou, A. Nairan, Y. Q. Zhang, J. X. Liu, K. W. Liu, S. Y. Hu, F. Y. Kang, H. J. Fan and C. Yang, *Energy Environ. Sci.*, 2020, **13**, 86–95.
10 P. S. Li, M. Y. Wang, X. X. Duan, L. R. Zheng, X. P. Cheng, Y. F. Zhang, Y. Kuang, Y. P. Li, Q. Ma, Z. X. Feng, W. Liu and X. M. Sun, *Nat. Commun.*, 2019, **10**, 1711.
11 Z. Wu, J. Yang, W. Shao, M. Cheng, X. Luo, M. Zhou, S. Li, T. Ma, C. Cheng and C. Zhao, *Adv. Fiber Mater.*, 2022, **4**, 774–785.
12 Y. Liao, R. He, W. Pan, Y. Li, Y. Wang, J. Li and Y. Li, *Chem. Eng. J.*, 2023, **464**, 142669.
13 W. Wang, J. Wang, S. Zhang, X. Song and B. Ma, *J. Mater. Chem. A*, 2022, **10**, 12334–12340.
14 F. Zhao, X. Mao, X. Zheng, H. Liu, L. Zhu, W. Li, Z. Wang and H. Chen, *J. Mater. Chem. A*, 2023, **11**, 276–286.
15 P. Yan, Q. Liu, H. Zhang, L. Qiu, H. B. Wu and X.-Y. Yu, *J. Mater. Chem. A*, 2021, **9**, 15586–15594.
16 W. T. Hong, M. Risch, K. A. Stoerzinger, A. Grimaud, J. Suntivich and Y. Shao-Horn, *Energy Environ. Sci.*, 2015, **8**, 1404–1427.
17 S. Dinda, A. Karmakar, D. Ghoshal and S. Kundu, *J. Mater. Chem. A*, 2024, **12**, 8392–8404.
18 Y. Umena, K. Kawakami, J.-R. Shen and N. Kamiya, *Nature*, 2011, **473**, 55–60.
19 S. Yuan, J. Peng, B. Cai, Z. Huang, A. T. Garcia-Esparza, D. Sokaras, Y. Zhang, L. Giordano, K. Akkiraju, Y. G. Zhu, R. Hübner, X. Zou, Y. Román-Leshkov and Y. Shao-Horn, *Nat. Mater.*, 2022, **21**, 673–680.
20 A. J. Howarth, Y. Liu, P. Li, Z. Li, T. C. Wang, J. T. Hupp and O. K. Farha, *Nat. Rev. Mater.*, 2016, **1**, 15018.
21 S. Kitagawa and R. Matsuda, *Coord. Chem. Rev.*, 2007, **251**, 2490–2509.
22 M. J. Van Vleet, T. Weng, X. Li and J. R. Schmidt, *Chem. Rev.*, 2018, **118**, 3681–3721.
23 J. Zhou and B. Wang, *Chem. Soc. Rev.*, 2017, **46**, 6927–6945.
24 J. L. Liu, D. D. Zhu, C. X. Guo, A. Vasileff and S. Z. Qiao, *Adv. Energy Mater.*, 2017, **7**, 1700518.
25 B. Zhang, Y. J. Zheng, T. Ma, C. D. Yang, Y. F. Peng, Z. H. Zhou, M. Zhou, S. Li, Y. H. Wang and C. Cheng, *Adv. Mater.*, 2021, **33**, 2006042.
26 X. Hou, Z. Han, X. Xu, D. Sarker, J. Zhou, M. Wu, Z. Liu, M. Huang and H. Jiang, *Chem. Eng. J.*, 2021, **418**, 129330.
27 Y. Liu, S. Deng, S. Fu, X. Wang, G. Liu and H. Yang, *J. Mater. Chem. A*, 2024, **12**, 8885–8892.
28 A. I. Nguyen, K. M. Van Allsburg, M. W. Terban, M. Bajdich, J. Oktawiec, J. Amtawong, M. S. Ziegler, J. P. Dombrowski, K. V. Lakshmi, W. S. Drisdell, J. Yano, S. J. L. Billinge and T. D. Tilley, *Proc. Natl. Acad. Sci. U. S. A.*, 2019, **116**, 11630–11639.
29 W. Zheng and L. Y. S. Lee, *ACS Energy Lett.*, 2021, **6**, 2838–2843.
30 H. Jiang, X. C. Liu, Y. Wu, Y. Shu, X. Gong, F. S. Ke and H. Deng, *Angew. Chem., Int. Ed.*, 2018, **57**, 3916–3921.
31 J. Du, F. Li and L. Sun, *Chem. Soc. Rev.*, 2021, **50**, 2663–2695.
32 X. Shen, L. Huang, S. Li, L. Tang, Q. Lei, B. Zhao, H. Hao, W. Li, M. Zeng and G. He, *Dalton Trans.*, 2023, **52**, 17711–17716.
33 Y. Wu, Y. Li, J. Gao and Q. Zhang, *SusMat*, 2021, **1**, 66–87.
34 C. Zhao, Z. Jiang, Y. Liu, Y. Zhou, P. Yin, Y. Ke and H. Deng, *J. Am. Chem. Soc.*, 2022, **144**, 23560–23571.
35 Z. Jiang, X. Xu, Y. Ma, H. S. Cho, D. Ding, C. Wang, J. Wu, P. Oleynikov, M. Jia, J. Cheng, Y. Zhou, O. Terasaki, T. Peng, L. Zan and H. Deng, *Nature*, 2020, **586**, 549–554.
36 X. Zhao, P. Pachfule, S. Li, J. R. J. Simke, J. Schmidt and A. Thomas, *Angew. Chem., Int. Ed.*, 2018, **57**, 8921–8926.
37 Z. Xue, Y. Li, Y. Zhang, W. Geng, B. Jia, J. Tang, S. Bao, H. P. Wang, Y. Fan, Z. w. Wei, Z. Zhang, Z. Ke, G. Li and C. Y. Su, *Adv. Energy Mater.*, 2018, **8**, 1801564.
38 M. Ma, A. Bétard, I. Weber, N. S. Al-Hokbany, R. A. Fischer and N. Metzler-Nolte, *Cryst. Growth Des.*, 2013, **13**, 2286–2291.
39 Y.-S. Wei, M. Zhang, P.-Q. Liao, R.-B. Lin, T.-Y. Li, G. Shao, J.-P. Zhang and X.-M. Chen, *Nat. Commun.*, 2015, **6**, 8348.
40 C. Scherb, R. Koehn and T. Bein, *J. Mater. Chem.*, 2010, **20**, 3046–3051.
41 S. Li, B. B. Chen, Y. Wang, M. Y. Ye, P. A. van Aken, C. Cheng and A. Thomas, *Nat. Mater.*, 2021, **20**, 1240–1247.
42 B. Zhang, Z. Wu, W. Shao, Y. Gao, W. Wang, T. Ma, L. Ma, S. Li, C. Cheng and C. Zhao, *Angew. Chem., Int. Ed.*, 2022, **61**, e202115331.
43 F. Cheng, Z. Li, L. Wang, B. Yang, J. Lu, L. Lei, T. Ma and Y. Hou, *Mater. Horiz.*, 2021, **8**, 556–564.
44 M. Zhuansun, Y. Liu, R. Lu, F. Zeng, Z. Xu, Y. Wang, Y. Yang, Z. Wang, G. Zheng and Y. Wang, *Angew. Chem., Int. Ed.*, 2023, **62**, e202309875.

45 C. Hu, Y. Hu, C. Fan, L. Yang, Y. Zhang, H. Li and W. Xie, *Angew. Chem., Int. Ed.*, 2021, **60**, 19774–19778.
46 Y. Zhang, W. Zheng, H. Wu, R. Zhu, Y. Wang, M. Wang, T. Ma, C. Cheng, Z. Zeng and S. Li, *SusMat*, 2023, **4**, 106–115.
47 L. Yu, H. Zhou, J. Sun, F. Qin, F. Yu, J. Bao, Y. Yu, S. Chen and Z. Ren, *Energy Environ. Sci.*, 2017, **10**, 1820–1827.
48 G. F. Chen, T. Y. Ma, Z. Q. Liu, N. Li, Y. Z. Su, K. Davey and S. Z. Qiao, *Adv. Funct. Mater.*, 2016, **26**, 3314–3323.
49 L. Huang, D. Chen, G. Luo, Y. R. Lu, C. Chen, Y. Zou, C. L. Dong, Y. Li and S. Wang, *Adv. Mater.*, 2019, **31**, 1901439.